

Early Accretion of Large Amount of Solids for Directly-Imaged Exoplanets

Ji WANG (王吉) ¹

¹*Department of Astronomy, The Ohio State University, 100 W 18th Ave, Columbus, OH 43210 USA*

(Received October 3, 2023; Revised; Accepted)

Submitted to ApJ

ABSTRACT

As the number of planetary mass objects (PMOs, $\lesssim 13 M_{\text{Jupitr}}$) at wider separation ($\gtrsim 10$ AU) grows, there is emerging evidence that they form differently from their higher-mass brown-dwarf (BD) counterparts. Namely, PMOs' atmospheres are enriched by metals which is usually interpreted as a sign of solid accretion. This points to the formation channel through core accretion. However, there has hitherto been no quantitative analysis at population level to investigate the amount and timing of solid accretion. Here, we analyze a sample of five directly-imaged exoplanets with measured stellar and planetary chemical abundances (51 Eri b, β Pic b, HIP 65426 b, and HR 8799 c and e). We show that these PMOs accrete large amount of solids regardless of formation channels. On average $\gtrsim 100 M_{\oplus}$ solids (ranging from 98.6 to 845.2 M_{\oplus} for individual systems) are accreted to enrich planet atmospheres if forming via core accretion whereas the solid accretion needs to be $\gtrsim 20 M_{\oplus}$ (ranging from 22.4 to 782.3 M_{\oplus}) if forming via gravitational instability. The result implies that the solid accretion process has to happen at an early stage (< 1 Myr) when large amount of solids are available in young protoplanetary disks.

1. INTRODUCTION

As the population of directly imaged exoplanets continues to grow, there is an increasing interest in their formation origin and accretion history. There are two ways of forming planetary mass objects, a companion can form through gravitational instability (GI) in disks (Boss 1997). Alternatively, a companion can form in a proto-planetary disk through core accretion (CA, Pollack et al. 1996).

There is suggestive evidence that planetary-mass companions and their higher-mass counterparts brown dwarfs (BDs) form through distinct mechanisms (Fig. 1). All directly-imaged exoplanets have super-stellar metallicities, which suggests accretion of solids rich in Carbon (C) and Oxygen (O) that leads to super-stellar metallicities (Mollière et al. 2020; Wang et al. 2023). In contrast, the higher-mass counterparts—BDs—show atmospheric metallicities that are consistent with stellar values, indicating a multiple-star formation channel in which each component inherits a cloud/filament that is chemically identical.

Corresponding author: Ji Wang
wang.12220@osu.edu

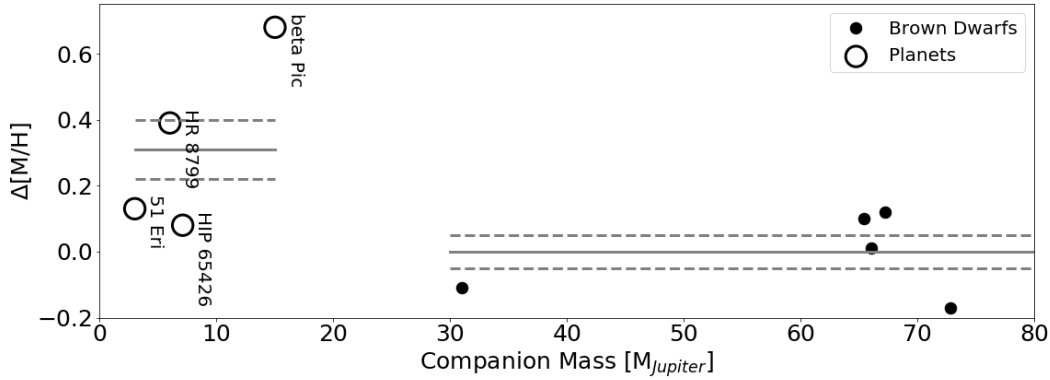


Figure 1. Directly-imaged exoplanets have super-stellar metallicities whereas higher-mass brown dwarf (BD) have stellar metallicities. The average relative metallicity ($\Delta[M/H]$) of directly-imaged exoplanets (open circles, HR 8799 c and e are shown as one data point for plotting clarity) is 0.32 ± 0.09 dex (grey horizontal lines). $\Delta[M/H]$ is the difference between the planet atmospheric metallicity and stellar metallicity. The error bar is the standard deviation divided by \sqrt{N} , where $N=5$ is the number of directly-imaged exoplanet systems. In comparison, the average metallicity of BDs (filled circles) is 0.00 ± 0.05 dex (grey horizontal lines). The five benchmark BDs are Gl 570 D, HD 3651 B (Line et al. 2015), HD 19467 B (Maire et al. 2020), HR 7672 B (Wang et al. 2022), and HD 4747 B (Xuan et al. 2022).

Accretion history, regardless of forming through GI or CA, plays a critical role in the metal enrichment of directly imaged exoplanets. Previous studies show that a solid accretion mass of $\sim 100 M_{\oplus}$ is needed to explain the atmospheric metal enrichment for β Pic b (GRAVITY Collaboration et al. 2020), HR 8799 c (Wang et al. 2023) and e (Mollière et al. 2020). This is puzzling because such a large mass reservoir may only be possible when the disk is young, which points to a very early planet formation (< 1 Myr). Such an early planet formation is usually consistent with the GI channel, but recent works under the CA paradigm also show that that forming planets within 1 Myr is possible via early formation of solid cores, such as planetesimals by the streaming instability (e.g., Youdin & Goodman 2005; Li & Youdin 2021), or embryos in self-gravitating disks (Baehr et al. 2022), and then subsequent pebble accretion (Ormel & Klahr 2010; Johansen & Lambrechts 2017; Baehr 2023).

It is therefore still unclear via which dominant mechanism the directly-imaged exoplanets

form, and how much solid mass has been accreted onto the planets depending on the formation mechanism and location. This paper aims to address these questions using a Bayesian inference framework. We organize the paper as follows. §2 summarizes the collected data. §3 presents our model and the Bayesian framework. Main results are in §4. Discussions are provided in §5. A summary of the paper can be found in §6.

2. DATA

The data for the five exoplanets in four systems are presented in Table 1. Our selection criteria require that the companion masses are below $13 M_{\text{Jupiter}}$ and their metallicity and C/O have been reported. In addition, we also include solar system gas giant planets, Jupiter and Saturn, for a comparative study (§5.1). The abundances for solar system planets are obtained from Atreya et al. (2018).

3. METHOD

3.1. Setting the Stage

The number of element X, we denote as N_X , can be calculated as follows:

$$N_X = \frac{n_{X,s}}{f_{sg}} M_s + \frac{n_{X,g}}{1+f_{sg}} M_g, \quad (1)$$

where $n_{X,s}$ and $n_{X,g}$ are the number of X atoms per unit disk mass in solid and gas phase, f_{sg} is solid to gas ratio, and M_s and M_g are the mass in solid and gas phase, respectively.

To calculate the mole ratio of the element X and H, for which we denote as X/H, for a planetary atmosphere that accretes some mass including M_s and M_g , we have:

$$\left(\frac{X}{H}\right)_{atm} = \frac{N_X}{N_H} = \frac{\frac{n_{X,s}}{f_{sg}} M_s + n_{X,g} M_g}{\frac{n_{H,s}}{f_{sg}} M_s + n_{H,g} M_g}. \quad (2)$$

Adopting the terminology in Öberg et al. (2011), the relative abundance α_X is:

$$\begin{aligned} \alpha_X &= \frac{\left(\frac{X}{H}\right)_{atm}}{\left(\frac{X}{H}\right)_*} \\ &= \frac{\frac{\frac{n_{X,s}}{f_{sg}} M_s + n_{X,g} M_g}{\frac{n_{H,s}}{f_{sg}} M_s + n_{H,g} M_g}}{\frac{n_X}{n_H}} \\ &= \frac{\frac{f_{X,s}}{f_{sg}} M_s + f_{X,g} M_g}{\frac{f_{H,s}}{f_{sg}} M_s + f_{H,g} M_g}, \end{aligned} \quad (3)$$

where n_X and n_H are the number of X and H atoms per unit mass (the ratio of the two is by definition stellar mole ratio), $f_{X,s}$ and $f_{X,g}$ are the fraction of element X in solid and gas phase, and $f_{H,s}$ and $f_{H,g}$ are the fraction of hydrogen in solid and gas phase. We then assume the fraction of H in solid phase (i.e., $f_{H,s}$) is negligible because H_2 , the most abundant materials, should be always in gas state under disk conditions. Given the assumption, the above equation becomes:

$$\alpha_X = \frac{f_{X,s}}{f_{sg}} \frac{M_s}{M_g} + (1 - f_{X,s}), \quad (4)$$

which is the same with Eq. 2 in Öberg et al. (2011).

3.2. Model Input and Output

We adopt the values in Table 2 for major C and O carriers in a proto-planetary disk. The planet atmospheric chemical composition, which is parameterized as α_C , α_O , and C/O, is determined by (1) where the planet forms; (2) how it forms; and (3) the amount of solid accretion. These parameters are compared to the observed values to infer the formation location, mechanism, and the accretion history. In addition, values in Table 2 are scaled to matched the observed host star values. C and O are given a different scaling factor to account for the non-solar C/O ratios.

Table 3 summarizes the input and output of our model. There are six input parameters: stellar C and O abundances as defined as $\xi_C = 12 + \log n_C$ and $\xi_O = 12 + \log n_O$, and C/O, planetary relative metallicity to the host star, i.e., $[M/H]_p - [M/H]_*$ and planetary atmospheric C/O. The parameters to be inferred are: scaling factor for stellar C and O abundances, planetary mass, mass of accreted solids, solid-to-gas ratio f_{sg} , formation mechanism, and the disk temperature where a planet forms which indicates the planet formation location.

Table 3 also provides equations that connect different parameters. For example, the scaling factors for stellar C and O abundances are used together with the C and O carrier abundances in Table 2 to match with stellar ξ_C , ξ_O and C/O. Specifically, ξ_C is calculated by $12 + \log \epsilon_C \sum n_{C_i}$, where ϵ_C is the scaling factor and n_{C_i} is each row in Table 2. ξ_O is similarly calculated, and $C/O = \epsilon_C \sum n_{C_i} / \epsilon_C \sum n_{O_i}$.

The planetary mass (M_P), mass of accreted solids, solid-to-gas ratio f_{sg} , formation mechanism, and the disk temperature (T_d) are used for calculating planet relative metallicity and C/O. Below we describe how that is done.

Using C as an example, for a given T_d , we can determine the phase (solid vs. gas) for each C carrier in Table 2. The fraction of C in solid

phase, $f_{C,s}$ in Eq. 4 is then calculated. In order for α_C to be determined, we explore a range of f_{sg} values from 0.01 to 0.10, which roughly cover the observed values for proto-planetary disks (Ansdell et al. 2016). The gas mass M_g is calculated by multiplying $M_P - M_S$ by $1/(1 + f_{sg})$ assuming all gas is acquired prior to the solid accretion stage. The mass of accreted solids M_s is calculated under two conditions depending on the chosen formation mechanism. For CA, M_s is the purely the accreted solids. For GI, M_s is the sum of the accreted solid mass and $(M_P - M_s) \cdot f_{sg}/(1 + f_{sg})$. Unlike the CA case in which solids are in the planetary core and do not contribute to the atmospheric metallicity, the GI case assumes that solids during the formation process are still perfectly mixed in the atmosphere. If this is not the case, then the required mass of solid accretion for GI will increase. The amount of the increase depends on how much of the accreted solid settles to form a core or become invisible to atmospheric measurements.

With $f_{C,s}$, f_{sg} , M_s , and M_g , C abundance α_C is determined via Eq. 4. O abundance α_O is determined in a similar way. To compared to the observed planet relative metallicity to the host star, i.e., $[M/H]_p - [M/H]_*$, we use the average of α_C and α_O , i.e., $\log((\alpha_C + \alpha_O)/2)$. To compare to the observed C/O, we use $\alpha_C/\alpha_O \times C/O_*$, where C/O_* is $\epsilon_C \sum n_{C_i}/\epsilon_C \sum n_{O_i}$ as noted in Table 3.

3.3. Bayesian Sampling and Model Selection

We compare the model output to the input data (listed in Table 1) in order to infer parameters such as accreted solid mass and formation mechanism (listed in full in Table 3). The priors for inferred parameters are given in Table 4. The likelihood function we use is: $-\frac{1}{2} \sum_{i=1}^n (\mathcal{D}_i - \mathcal{M}_i)^2/\mathcal{E}_i^2 - \frac{1}{2} \sum_{i=1}^n \ln(2\pi\mathcal{E}_i^2)$, where subscript i is parameter index, D is data, M is model, and ϵ is error. We used

PyMultiNest (Buchner et al. 2014) to sample posteriors and calculate evidence. Examples of retrieving accretion mass can be found in B.

4. RESULTS

4.1. Mass of Accreted Solids

Mass of Accreted Solids is inferred in our Bayesian modeling (§3.2) and is presented in Table 5. For the CA scenario, a planet accreted $\gtrsim 100 M_\oplus$ solids on average, with a noticeable outlier of β Pic b which accretes $\sim 1000 M_\oplus$ solids (Fig. 2). For the GI scenario, the required solid accretion is lower at $\sim 20 M_\oplus$.

Accretion of solids can be challenging once a gap is opened for the GI scenario (Helled & Schubert 2009). The typical time scale for efficient solid accretion is from 10^3 to 10^5 years (Bodenheimer et al. 1980). Accretion of $\sim 20 M_\oplus$ in this time scale requires a large inflow of solids that is at least $200 M_\oplus$ per Myr, which can only happen when the disk is young and massive at $\lesssim 1$ Myr (Tychoniec et al. 2020; Bosman et al. 2023).

However, a more severe challenge for GI, as noted in Wang et al. (2023), is forming multi-planetary systems because the turbulent nature unusually results in a single companion rather than multiple companions. While recent simulation shows that forming multiple intermediate mass planets is possible through the GI mechanism (Deng et al. 2021). It remains unclear if the similar mechanism can form systems with multiple gaseous giant planets such as the HR 8799 and β Pic systems. The multiple planets in these systems also exacerbate the mass budget issue as more than one planetary atmosphere need to be enriched.

In contrast, for the CA scenario, the accreted mass is $\gtrsim 100 M_\oplus$, which is much higher than the GI scenario. This is because the metals are locked in the core and atmospheric metal enrichment relies entirely on the subsequent solid accretion, whereas the atmospheric metal enrich-

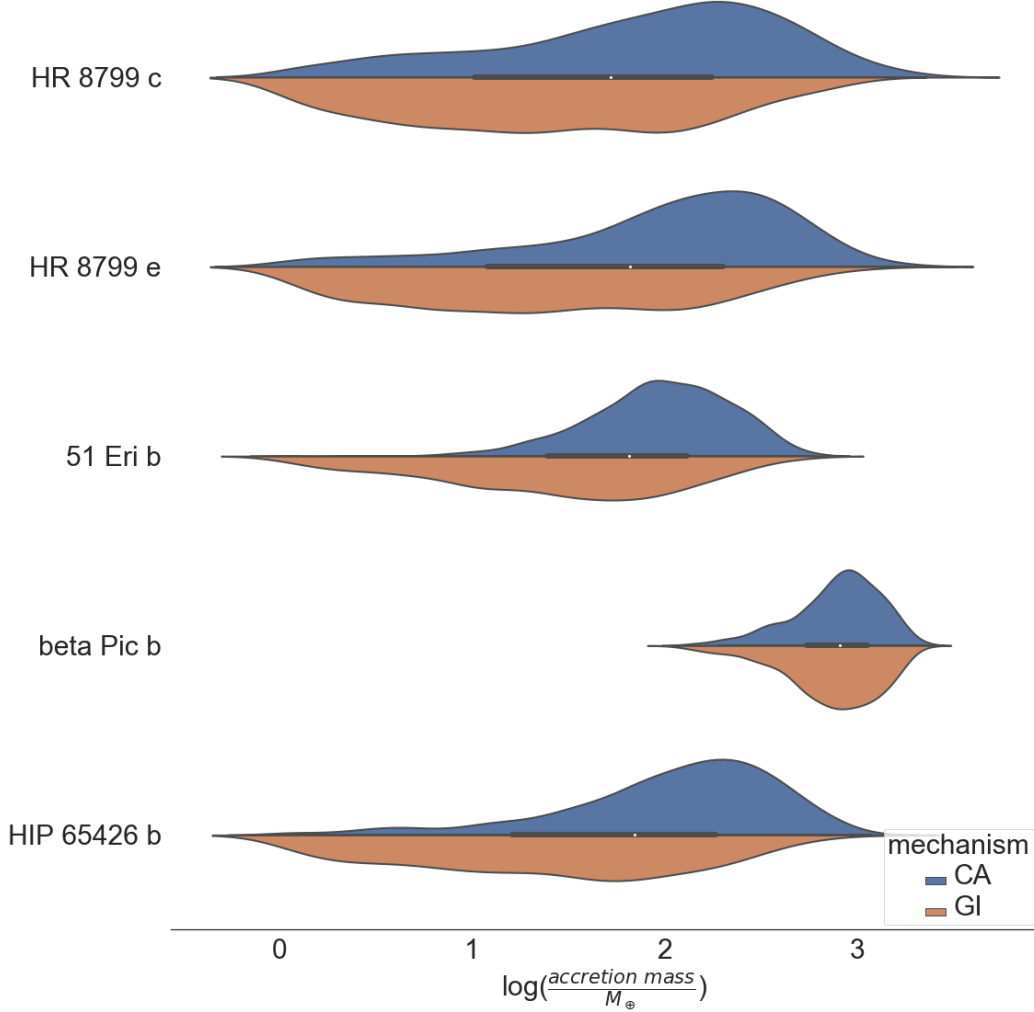


Figure 2. Directly-imaged exoplanets accrete on average $\gtrsim 100 M_{\oplus}$ solids to enrich their atmospheres if forming via CA whereas they would accrete $\sim 20 M_{\oplus}$ solids if forming via GI. Each row shows the inferred accretion mass for one directly-imaged exoplanet in two scenarios: CA (blue) and GI (orange). The median of the overall distribution (i.e., CA and GI) is represented by the white point, and the 25% and 75% percentiles are represented by the thick line.

ment in the GI scenario is aided by the initial metal content due to the assumption that solids during the formation are still perfectly mixed in the atmosphere.

4.2. Timing of the Solid Accretion

The large amount of accreted solids is difficult to be explained by the solid mass budget of a typical disk. At 1% disk mass ratio with a solar metallicity, the solid mass budget is $\sim 60 M_{\oplus}$, which is not enough for CA and barely suf-

ficient for GI for multiple planet systems even assuming 100% accretion efficiency.

The timing of the solid accretion needs to be early when disk mass ratio is higher and there is sufficient amount of inward drifting solids. Indeed, to facilitate early planet embryo and core formation within 1 Myr, most simulations assume $\sim 5\%$ disk mass ratio (e.g., Savvidou & Bitsch 2023; Baehr 2023). In addition, recent observations show that the pebble drift rate can be from 100 to more than $1000 M_{\oplus}$ per Myr at an early phase of a protoplanetary disk (~ 1

Myr, [Bosman et al. 2023](#)). Therefore, there should be sufficient solids available even though the accretion time scale is between 0.1 and 1 Myr. Moreover, it has been shown that planet formation can proceed at <0.5 Myr ([Segura-Cox et al. 2020](#)), so it is plausible for the accretion of solids through streamers in the class-0 or I envelope phase ([Visser et al. 2009](#)). Indeed, the observed dust masses for Class 0 disks ([Tychoniec et al. 2020](#)) are comparable to what we infer for solid accretion at $\sim 100 M_{\oplus}$. All the observational evidence and state-of-the-art simulations support that the timing of the solid accretion needs to be comparable or earlier than 1 Myr in order to meet the accretion mass budget.

5. DISCUSSION

5.1. *Jupiter and Saturn*

To test the validity, we apply our inference framework to the solar system gas giant planets, Jupiter and Saturn.

For the CA mechanism, the accreted solid mass shows a bimodal distribution with two preferred formation locations: within the H_2O iceline and beyond the CO iceline (see Fig. 4 in §A). The accreted mass for formation within the H_2O iceline is about twice higher than formation beyond the CO iceline ($111 M_{\oplus}$ vs. $54 M_{\oplus}$) for Jupiter. Here, we report the result for the formation location beyond the CO iceline in Table 5 at $54.7_{-26.5}^{+24.2} M_{\oplus}$ because formation beyond the CO iceline is more consistent with previous claim of formation beyond N_2 iceline ([Öberg & Wordsworth 2019](#)). Saturn, similarly showing a bimodal distribution of inferred accretion mass, accreted $29.5_{-11.2}^{+9.8} M_{\oplus}$ if forming beyond the CO iceline. Our results are broadly consistent within $1\text{-}\sigma$ when compared to previous works ([Guillot 1999](#); [Thorngrén et al. 2016](#)).

We now attempt to address the abnormally high required accretion mass if Jupiter formed within the H_2O iceline. If that is the case, then the inferred accretion mass is $111.4_{-44.2}^{+41.3} M_{\oplus}$.

M_{\oplus} . This issue can be alleviated by invoking the pebble evaporation mechanism ([Schneider & Bitsch 2021](#); [Bitsch & Mah 2023](#)). Evaporating pebbles, especially in the inner disk where temperature is high, can enhance the local gas metallicity and therefore enrich the planet atmospheric metallicity during the gas accretion process. Combining pebble evaporation and solid accretion to explain the metallicity enrichment will reduce the mass requirement for solid accretion alone.

For GI, which is not favored for the solar system formation (e.g., [Kruijer et al. 2017](#)), the accreted solid mass again shows a bimodal distribution with two preferred formation locations. Assuming forming beyond the CO iceline, the accreted solid mass for Saturn is $28.3_{-11.3}^{+7.7} M_{\oplus}$ (see also Table 5), which is consistent with literature values: $20\text{-}30 M_{\oplus}$ ([Guillot 1999](#)) and $27 \pm 8 M_{\oplus}$ ([Thorngrén et al. 2016](#)). For Jupiter, the accreted mass is $39.2_{-18.0}^{+24.2} M_{\oplus}$. Within the uncertainty, these numbers are also consistent with the total metal content estimation of $10\text{-}40 M_{\oplus}$ from [Guillot \(1999\)](#) and $37 \pm 20 M_{\oplus}$ from [Thorngrén et al. \(2016\)](#).

5.2. *Comparing to Previous Results*

5.2.1. *β Pic b*

[GRAVITY Collaboration et al. \(2020\)](#) adopt a similar approach to investigate solid accretion history for β Pic b. The major differences between their approach and this work are (1) we consider both $[M/H]$ and C/O while they consider only C/O; and (2) we use a Bayesian inference framework taking fully into consideration of measurement uncertainties. While [GRAVITY Collaboration et al. \(2020\)](#) conclude that β Pic b is unlikely to form via the gravitational instability mechanism because of unusually long time for the pre-collapse phase, or an extremely efficient accretion (with an accretion rate of $4000 M_{\oplus}$ per Myr), we note that a pebble influx rate as high as $1000 M_{\oplus}$ per Myr has

been observationally supported (Bosman et al. 2023). Therefore, forming β Pic b through gravitational instability is still a plausible channel.

Core accretion scenario for β Pic b has also been considered in GRAVITY Collaboration et al. (2020). They calculate that 80-150 M_{\oplus} needs to be accreted to reach the 1- σ upper limit of C/O measurement. In comparison, this work infer $\sim 1000 M_{\oplus}$ needs to be accreted in order to explain the observed C/O and planet metallicity. We also find that formation within the H₂O iceline is slightly preferred compared to other locations: the posterior sample number ratio is about 3:1 for formation within H₂O iceline versus formation at other locations.

5.2.2. HR 8799 c and e

HR 8799 c (Wang et al. 2023) and e (Mollière et al. 2020) are found to be metal enriched. In the core accretion scenario, it is estimated that a solid mass of $\sim 100 M_{\oplus}$ needs to be accreted (Mollière et al. 2020). This is consistent with our findings in this work (see Fig. 2 and Table 5). The challenge for HR 8799 planets is to explain how solids can overcome potential traps and gaps in protoplanetary disk to reach planet c and e. This warrants future investigations.

5.3. Mass-Metallicity Relationship for Transiting and Directly-Imaged Exoplanets

Thorngren et al. (2016) study a sample of transiting planets with low stellar irradiation and report a positive mass-metallicity relation, i.e., the mass of heavy element (M_Z) scales with planet mass M with a power law of ~ 0.6 , which is consistent the prediction of the CA model. They also concluded that metal-enriched giant planet atmospheres should be the rule because the heavy metal mass for giant planets greatly exceeds the core mass and should therefore enrich the atmospheric metallicity.

In this work, we significantly increase the sample on the higher mass end by including the five directly-imaged exoplanets. We show in Fig. 3 that the mass-metallicity relation still holds at the highest end in the planetary mass regime and extends from the transiting exoplanet population to the directly-imaged exoplanets.

6. SUMMARY

We provide evidence that solid accretion takes place early when the disk is massive and younger than ~ 1 Myr, which is corroborative with state-of-the-art observations and simulations. In reaching this conclusion, we develop a Bayesian framework (§3) to infer the total mass mass of solid accretion along with other parameters that we marginalize (see Table 4). The framework is validated using the solar system gas giant planets: Jupiter and Saturn (§5.1) by finding consistent total metal contents with literature values (Table 5). Our results are also compared to previous studies for individual systems (§5.2) to demonstrate the improvement of methodology, namely, going beyond C/O to include [M/H] and treating uncertainties in a Bayesian framework.

As such, we summarize our major findings here. We analyze a sample of five directly-imaged exoplanets with measured stellar and planetary chemical abundances (51 Eri b, β Pic b, HIP 65426 b, and HR 8799 c and e). We infer a large amount of accreted solids to enrich their atmospheres regardless of formation channels. On average $\gtrsim 100 M_{\oplus}$ solids (ranging from 98.6 to 845.2 M_{\oplus} for individual systems) are accreted to enrich planet atmospheres if forming via core accretion whereas the solid accretion needs to be $\gtrsim 20 M_{\oplus}$ (ranging from 22.4 to 782.3 M_{\oplus}) if forming via gravitational instability. The result implies that the solid accretion process has to happen at early stage (< 1 Myr) when large amount of solids are available.

Future improvement of this work will come from two angles. First, ~ 20 -30 directly-imaged

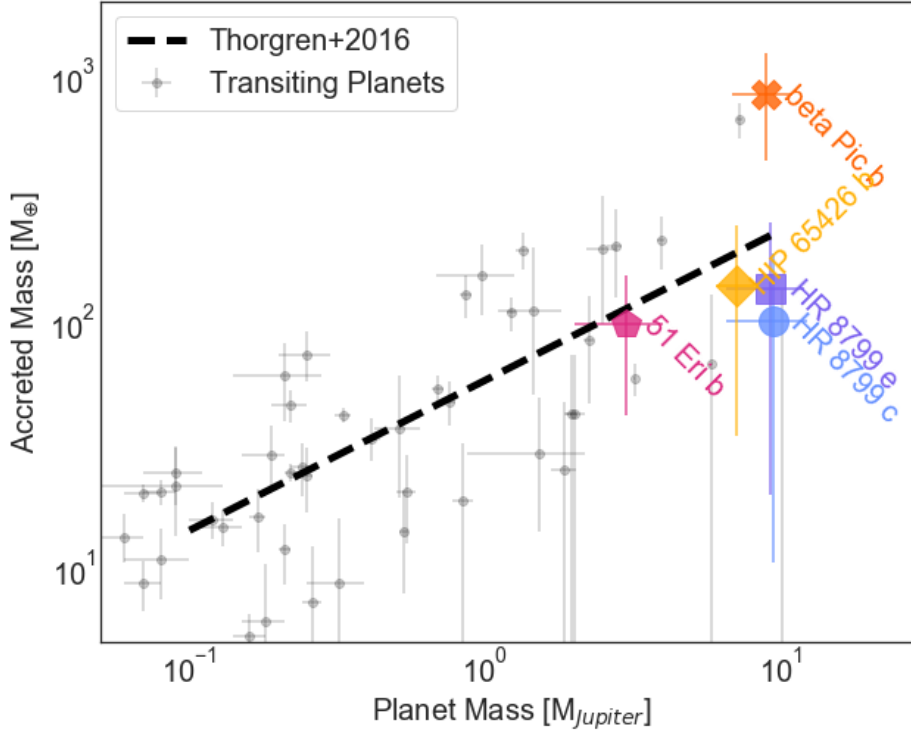


Figure 3. Directly-imaged exoplanets (colored symbols assuming core accretion) follow the same trend as the mass-metallicity relation for transiting exoplanets. Dashed line is the mass-metallicity relation reported in Thorgren et al. (2016) and the grey data points are transiting exoplanets used in deriving the the relation.

exoplanets will be characterized by facilities such as JWST, the Keck Planet Imager and Characterizer (KPIC, Mawet et al. 2018; Jovanovic et al. 2019; Delorme et al. 2020, 2021), and VLT/HiRISE (Vigan et al. 2018; El Morsy et al. 2022). Our Bayesian framework is ideal to include more objects with data of chemical abundances and elemental ratios. Second, the measurement uncertainty for planetary atmospheric composition (Table 1) is expected to be much improved by the wavelength coverage of

JWST and the high-spectral resolution of KPIC and VLT/HiRISE, the precision of the inference will benefit from the improved measurement uncertainty, although the model in our Bayesian framework will need to be improved accordingly to limit the systematic modeling error.

Acknowledgments This work is supported by the National Science Foundation under Grant No. 2143400. The author would like to thank helpful comments and constructive conversations from Rixin Li, Scott Gaudi, and Eric Ford.

REFERENCES

- Ansdell, M., Williams, J. P., van der Marel, N., et al. 2016, *ApJ*, 828, 46,
doi: 10.3847/0004-637X/828/1/46
- Asplund, M., Grevesse, N., Sauval, A. J., & Scott, P. 2009, *ARA&A*, 47, 481,
doi: 10.1146/annurev.astro.46.060407.145222

- Atreya, S. K., Crida, A., Guillot, T., et al. 2018, in *Saturn in the 21st Century*, ed. K. H. Baines, F. M. Flasar, N. Krupp, & T. Stallard, 5–43, doi: [10.1017/9781316227220.002](https://doi.org/10.1017/9781316227220.002)
- Baehr, H. 2023, *MNRAS*, 523, 3348, doi: [10.1093/mnras/stad1564](https://doi.org/10.1093/mnras/stad1564)
- Baehr, H., Zhu, Z., & Yang, C.-C. 2022, *ApJ*, 933, 100, doi: [10.3847/1538-4357/ac7228](https://doi.org/10.3847/1538-4357/ac7228)
- Bitsch, B., & Mah, J. 2023, arXiv e-prints, arXiv:2309.00509, doi: [10.48550/arXiv.2309.00509](https://doi.org/10.48550/arXiv.2309.00509)
- Bochanski, J. J., Faherty, J. K., Gagné, J., et al. 2018, *AJ*, 155, 149, doi: [10.3847/1538-3881/aaaebe](https://doi.org/10.3847/1538-3881/aaaebe)
- Bodenheimer, P., Grossman, A. S., Decamp, W. M., Marcy, G., & Pollack, J. B. 1980, *Icarus*, 41, 293, doi: [10.1016/0019-1035\(80\)90012-3](https://doi.org/10.1016/0019-1035(80)90012-3)
- Bosman, A. D., Appelgren, J., Bergin, E. A., Lambrechts, M., & Johansen, A. 2023, *ApJL*, 944, L53, doi: [10.3847/2041-8213/acb651](https://doi.org/10.3847/2041-8213/acb651)
- Boss, A. P. 1997, *Science*, 276, 1836, doi: [10.1126/science.276.5320.1836](https://doi.org/10.1126/science.276.5320.1836)
- Brandt, G. M., Brandt, T. D., Dupuy, T. J., Li, Y., & Michalik, D. 2021a, *AJ*, 161, 179, doi: [10.3847/1538-3881/abdc2e](https://doi.org/10.3847/1538-3881/abdc2e)
- Brandt, G. M., Brandt, T. D., Dupuy, T. J., Michalik, D., & Marleau, G.-D. 2021b, *ApJL*, 915, L16, doi: [10.3847/2041-8213/ac0540](https://doi.org/10.3847/2041-8213/ac0540)
- Brown-Sevilla, S. B., Maire, A. L., Mollière, P., et al. 2022, arXiv e-prints, arXiv:2211.14330, doi: [10.48550/arXiv.2211.14330](https://doi.org/10.48550/arXiv.2211.14330)
- Buchner, J., Georgakakis, A., Nandra, K., et al. 2014, *A&A*, 564, A125, doi: [10.1051/0004-6361/201322971](https://doi.org/10.1051/0004-6361/201322971)
- Carter, A. L., Hinkley, S., Kammerer, J., et al. 2022, arXiv e-prints, arXiv:2208.14990, doi: [10.48550/arXiv.2208.14990](https://doi.org/10.48550/arXiv.2208.14990)
- Delorme, J.-R., Jovanovic, N., Echeverri, D., et al. 2020, in *Society of Photo-Optical Instrumentation Engineers (SPIE) Conference Series*, Vol. 11447, *Society of Photo-Optical Instrumentation Engineers (SPIE) Conference Series*, 114471P, doi: [10.1117/12.2562836](https://doi.org/10.1117/12.2562836)
- Delorme, J.-R., Jovanovic, N., Echeverri, D., et al. 2021, *Journal of Astronomical Telescopes, Instruments, and Systems*, 7, 035006, doi: [10.1117/1.JATIS.7.3.035006](https://doi.org/10.1117/1.JATIS.7.3.035006)
- Deng, H., Mayer, L., & Helled, R. 2021, *Nature Astronomy*, 5, 967, doi: [10.1038/s41550-021-01400-5](https://doi.org/10.1038/s41550-021-01400-5)
- Dupuy, T. J., Brandt, G. M., & Brandt, T. D. 2022, *MNRAS*, 509, 4411, doi: [10.1093/mnras/stab3148](https://doi.org/10.1093/mnras/stab3148)
- El Morsy, M., Vigan, A., Lopez, M., et al. 2022, *A&A*, 667, A171, doi: [10.1051/0004-6361/202243408](https://doi.org/10.1051/0004-6361/202243408)
- GRAVITY Collaboration, Nowak, M., Lacour, S., et al. 2020, *A&A*, 633, A110, doi: [10.1051/0004-6361/201936898](https://doi.org/10.1051/0004-6361/201936898)
- Guillot, T. 1999, *Planet. Space Sci.*, 47, 1183, doi: [10.1016/S0032-0633\(99\)00043-4](https://doi.org/10.1016/S0032-0633(99)00043-4)
- Helled, R., & Schubert, G. 2009, *ApJ*, 697, 1256, doi: [10.1088/0004-637X/697/2/1256](https://doi.org/10.1088/0004-637X/697/2/1256)
- Johansen, A., & Lambrechts, M. 2017, *Annual Review of Earth and Planetary Sciences*, 45, 359, doi: [10.1146/annurev-earth-063016-020226](https://doi.org/10.1146/annurev-earth-063016-020226)
- Jovanovic, N., Delorme, J. R., Bond, C. Z., et al. 2019, arXiv e-prints, arXiv:1909.04541, <https://arxiv.org/abs/1909.04541>
- Kruijer, T. S., Burkhardt, C., Budde, G., & Kleine, T. 2017, *Proceedings of the National Academy of Science*, 114, 6712, doi: [10.1073/pnas.1704461114](https://doi.org/10.1073/pnas.1704461114)
- Li, R., & Youdin, A. N. 2021, *ApJ*, 919, 107, doi: [10.3847/1538-4357/ac0e9f](https://doi.org/10.3847/1538-4357/ac0e9f)
- Line, M. R., Teske, J., Burningham, B., Fortney, J. J., & Marley, M. S. 2015, *ApJ*, 807, 183, doi: [10.1088/0004-637X/807/2/183](https://doi.org/10.1088/0004-637X/807/2/183)
- Maire, A. L., Molaverdikhani, K., Desidera, S., et al. 2020, *A&A*, 639, A47, doi: [10.1051/0004-6361/202037984](https://doi.org/10.1051/0004-6361/202037984)
- Mawet, D., Bond, C. Z., Delorme, J. R., et al. 2018, in *Society of Photo-Optical Instrumentation Engineers (SPIE) Conference Series*, Vol. 10703, *Adaptive Optics Systems VI*, ed. L. M. Close, L. Schreiber, & D. Schmidt, 1070306, doi: [10.1117/12.2314037](https://doi.org/10.1117/12.2314037)
- Mollière, P., Stolker, T., Lacour, S., et al. 2020, *A&A*, 640, A131, doi: [10.1051/0004-6361/202038325](https://doi.org/10.1051/0004-6361/202038325)
- Öberg, K. I., Murray-Clay, R., & Bergin, E. A. 2011, *ApJL*, 743, L16, doi: [10.1088/2041-8205/743/1/L16](https://doi.org/10.1088/2041-8205/743/1/L16)
- Öberg, K. I., & Wordsworth, R. 2019, *AJ*, 158, 194, doi: [10.3847/1538-3881/ab46a8](https://doi.org/10.3847/1538-3881/ab46a8)
- Ormel, C. W., & Klahr, H. H. 2010, *A&A*, 520, A43, doi: [10.1051/0004-6361/201014903](https://doi.org/10.1051/0004-6361/201014903)
- Petrus, S., Bonnefoy, M., Chauvin, G., et al. 2021, *A&A*, 648, A59, doi: [10.1051/0004-6361/202038914](https://doi.org/10.1051/0004-6361/202038914)

- Pollack, J. B., Hubickyj, O., Bodenheimer, P., et al. 1996, *Icarus*, 124, 62, doi: [10.1006/icar.1996.0190](https://doi.org/10.1006/icar.1996.0190)
- Savvidou, S., & Bitsch, B. 2023, arXiv e-prints, arXiv:2309.03807, doi: [10.48550/arXiv.2309.03807](https://doi.org/10.48550/arXiv.2309.03807)
- Schneider, A. D., & Bitsch, B. 2021, *A&A*, 654, A71, doi: [10.1051/0004-6361/202039640](https://doi.org/10.1051/0004-6361/202039640)
- Segura-Cox, D. M., Schmiedeke, A., Pineda, J. E., et al. 2020, *Nature*, 586, 228, doi: [10.1038/s41586-020-2779-6](https://doi.org/10.1038/s41586-020-2779-6)
- Swastik, C., Banyal, R. K., Narang, M., et al. 2021, *AJ*, 161, 114, doi: [10.3847/1538-3881/abd802](https://doi.org/10.3847/1538-3881/abd802)
- Thorngren, D. P., Fortney, J. J., Murray-Clay, R. A., & Lopez, E. D. 2016, *ApJ*, 831, 64, doi: [10.3847/0004-637X/831/1/64](https://doi.org/10.3847/0004-637X/831/1/64)
- Tychoniec, L., Manara, C. F., Rosotti, G. P., et al. 2020, *A&A*, 640, A19, doi: [10.1051/0004-6361/202037851](https://doi.org/10.1051/0004-6361/202037851)
- Vigan, A., Otten, G. P. P. L., Muslimov, E., et al. 2018, in *Society of Photo-Optical Instrumentation Engineers (SPIE) Conference Series*, Vol. 10702, *Ground-based and Airborne Instrumentation for Astronomy VII*, ed. C. J. Evans, L. Simard, & H. Takami, 1070236, doi: [10.1117/12.2313681](https://doi.org/10.1117/12.2313681)
- Visser, R., van Dishoeck, E. F., Doty, S. D., & Dullemond, C. P. 2009, *A&A*, 495, 881, doi: [10.1051/0004-6361/200810846](https://doi.org/10.1051/0004-6361/200810846)
- Wang, J., Kolecki, J. R., Ruffio, J.-B., et al. 2022, *AJ*, 163, 189, doi: [10.3847/1538-3881/ac56e2](https://doi.org/10.3847/1538-3881/ac56e2)
- Wang, J., Wang, J. J., Ruffio, J.-B., et al. 2023, *AJ*, 165, 4, doi: [10.3847/1538-3881/ac9f19](https://doi.org/10.3847/1538-3881/ac9f19)
- Wang, J. J., Graham, J. R., Dawson, R., et al. 2018, *AJ*, 156, 192, doi: [10.3847/1538-3881/aae150](https://doi.org/10.3847/1538-3881/aae150)
- Xuan, J. W., Wang, J., Ruffio, J.-B., et al. 2022, *ApJ*, 937, 54, doi: [10.3847/1538-4357/ac8673](https://doi.org/10.3847/1538-4357/ac8673)
- Youdin, A. N., & Goodman, J. 2005, *ApJ*, 620, 459, doi: [10.1086/426895](https://doi.org/10.1086/426895)

Table 1. Data for Each Exoplanet System

Name	Star				Planet	
	ξ_C	ξ_O	C/O*	$[\text{M}/\text{H}]_P - [\text{M}/\text{H}]_*$	C/O _P	M_P
51 Eri b	-3.44 ± 0.05^1	-3.18 ± 0.05	0.55 ± 0.10	0.13 ± 0.30	0.38 ± 0.09	$[2.0 \dots 4.0]^2$
β Pic b	-3.57 ± 0.05	-3.31 ± 0.05	0.55 ± 0.10^3	0.68 ± 0.10	0.43 ± 0.05^4	$[6.8 \dots 11.0]^5$
HIP 65426 b	-3.60 ± 0.05^6	-3.34 ± 0.05	0.55 ± 0.10^7	0.08 ± 0.25	0.40 ± 0.10^8	7.1 ± 1.1^9
HR 8799 c	-3.46 ± 0.12	-3.19 ± 0.14	0.54 ± 0.10^{10}	0.38 ± 0.30^{11}	0.67 ± 0.15^{11}	$[6.5 \dots 12.0]^{12}$
HR 8799 e				0.36 ± 0.25	0.60 ± 0.07^{13}	$[6.5 \dots 12.0]^{12}$
Jupiter	-3.57 ± 0.05	-3.31 ± 0.05	0.55 ± 0.10^3	0.61 ± 0.10^{14}	0.55 ± 0.15^{15}	$[0.9 \dots 1.1]^{16}$
Saturn				0.95 ± 0.03^{14}	0.55 ± 0.15^{15}	$[0.27 \dots 0.33]^{16}$

NOTE—1, Swastik et al. (2021), assuming solar C/O (Asplund et al. 2009) and scaled from $[\text{Fe}/\text{H}] = 0.13$, uncertainty is increased to 0.05; 2, Brown-Sevilla et al. (2022), using Table 5 “New nominal” column for planet parameters; 3, assuming solar values; 4, GRAVITY Collaboration et al. (2020), using values in the last row in Table 3, uncertainties are readjusted to 0.10 and 0.05 for metallicity and C/O; 5, lower limit from Brandt et al. (2021a) and upper limit from Dupuy et al. (2022); 6, Swastik et al. (2021); Bochanski et al. (2018); 7, assuming solar C/O (Asplund et al. 2009); 8, Petrus et al. (2021), using “K band with continuum” solution in Table 2, uncertainties are readjusted to 0.25 and 0.10 for metallicity and C/O; 9, Carter et al. (2022); 10, Wang et al. (2022), C/O uncertainty readjusted to 0.10; 11, Wang et al. (2023), use the average of $[\text{C}/\text{H}]$ and $[\text{O}/\text{H}]$ to calculate $[\text{M}/\text{H}]_P$, uncertainty readjusted to 0.30; 12, using the lower mass limit and the dynamical stability upper limit in Wang et al. (2018) which encompasses the mass range in Brandt et al. (2021b); 13, Mollière et al. (2020); 14, Atreya et al. (2018) using C/H as a approximation to M/H; 15, assuming solar C/O but with a larger uncertainty; 16, assuming 10% mass uncertainty.

Table 2. Adopted Properties for C and O Carriers

Species	T_{evap}	n_O	n_C
	[K]	$[10^{-4} \times n_H]$	$[10^{-4} \times n_H]$
CO	20	1.8	1.8
CO ₂	47	0.6	0.3
H ₂ O	135	0.9	...
Carbon grains	500	...	0.6
Silicate	1500	1.4	...

APPENDIX

A. CORNER PLOTS

B. DIAGNOSTIC PLOTS

Table 3. Inference Method

Input Data	Input Symbols	Parameters	Symbols	Equation
Stellar C abundance	ξ_C	C Scaling Factor	ϵ_C	$\xi_C = \log \epsilon_C \sum n_{C_i}^{**}$
Stellar O abundance	ξ_O	O Scaling Factor	ϵ_O	$\xi_O = \log \epsilon_O \sum n_{O_i}$
Stellar C/O	C/O_*	Planet Mass	M_P	$C/O_* = \epsilon_C \sum n_{C_i} / \epsilon_C \sum n_{O_i}$
Planet Relative Metallicity*	$[M/H]_P - [M/H]_*$	Accreted Solid Mass	M_s	$[M/H]_P - [M/H]_* =$ $\log((\alpha_C + \alpha_O)/2)^{***}$
Planetary C/O	C/O_P	Dust-to-Gas Ratio	f_{sg}	$C/O_P = \alpha_C / \alpha_O \times C/O_*$
		Disk Temperature	T_d	
		Formation Mechanism	...	

NOTE—*: If [C/H] and [O/H] are both available, then we use the average of the two. **: n_{C_i} can be found in the n_C column in Table 2. ***: α_X is calculated with Eq. 4.

Table 4. Parameters Used in the Bayesian Inference

Parameter	Unit	Type	Lower or Mean	Upper or Std
C Scaling Factor (ϵ_C)	...	Uniform	0.5	2.0
O Scaling Factor (ϵ_O)	...	Uniform	0.5	2.0
Planet Mass (M_P)	$M_{Jupiter}$	see Table 1 for individual planets		
Accreted Solid Mass ($\log M_s$)	M_\oplus	Log-uniform	0	4
Dust-to-Gas Ratio (f_{sg})	...	Uniform	0.01	0.05
Disk Temperature ($\log T_d$)	K	Log-uniform	1.0	2.5
Formation Mechanism	...	Uniform*	0	1

NOTE—*: [0.0-0.5) means core-accretion and [0.5-1.0) means gravitational instability.

Table 5. Mass of Metals in Jupiter, Saturn, and Directly-Imaged Exoplanets

Source	Jupiter [M_\oplus]	Saturn [M_\oplus]	HR 8799 c [M_\oplus]	HR 8799 e [M_\oplus]	51 Eri b [M_\oplus]	β Pic b [M_\oplus]	HIP 65426 b [M_\oplus]
Guillot (1999)	10-40	20-30
Thorngren et al. (2016)*	37 ± 20	27 ± 8
this work (GI)	$39.2^{+24.2}_{-18.0}$	$28.3^{+7.7}_{-11.3}$	$24.0^{+132.7}_{-20.4}$	$22.4^{+128.0}_{-19.1}$	$32.0^{+80.2}_{-26.2}$	$782.3^{+497.2}_{-361.8}$	$28.1^{+116.0}_{-24.4}$
this work (CA)**	$54.7^{+24.2}_{-26.5}$	$29.5^{+9.8}_{-11.2}$	$100.3^{+279.9}_{-89.8}$	$137.0^{+257.1}_{-117.2}$	$98.6^{+123.1}_{-56.9}$	$845.2^{+461.4}_{-390.2}$	$141.2^{+211.1}_{-106.6}$

NOTE—*: use larger uncertainties in Table 2 in Thorngren et al. (2016) **: core mass not included.

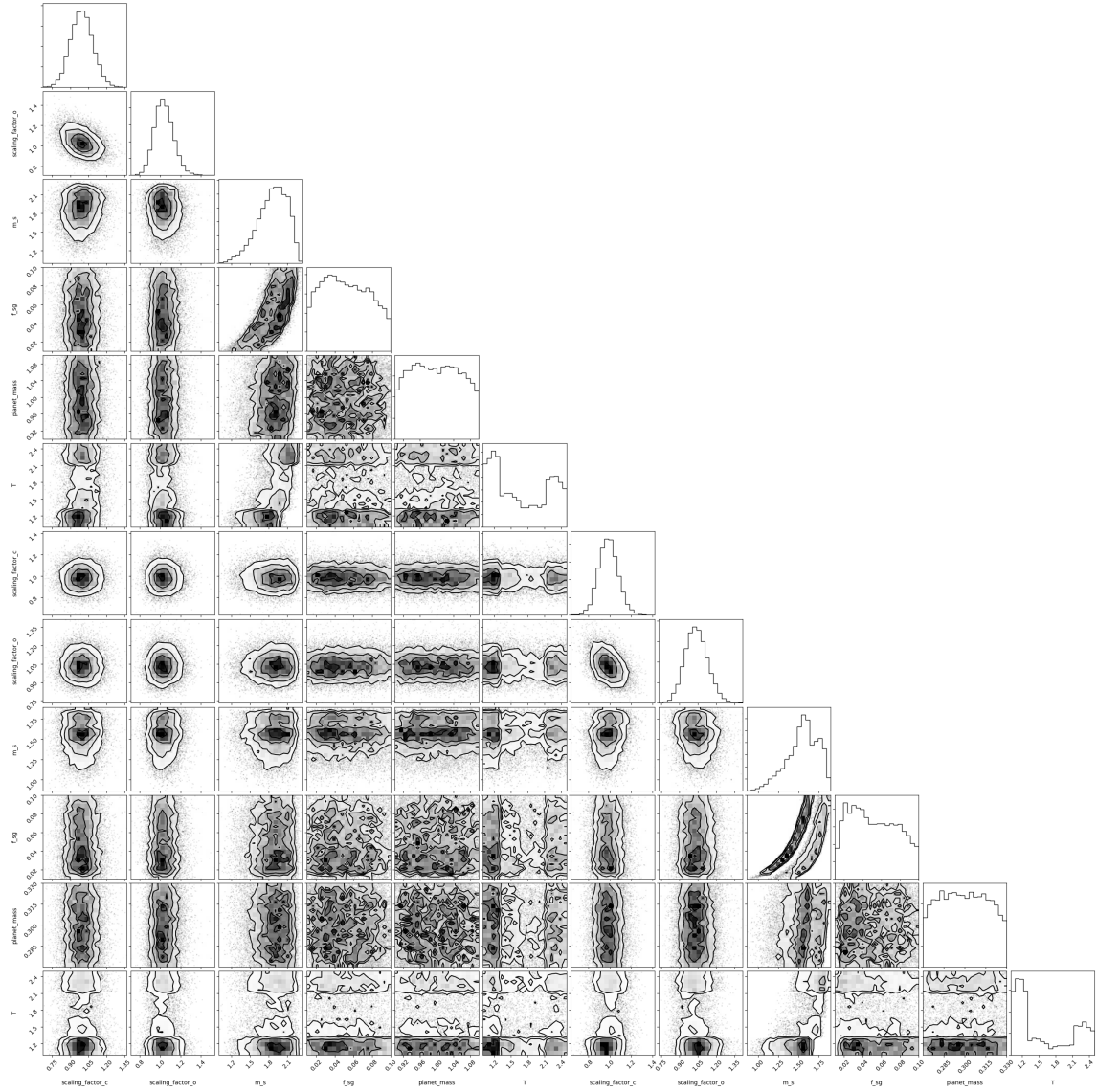


Figure 4. Corner plot for solar system gas giant planets forming via CA. The left six columns are for Jupiter and the right six columns are for Saturn.

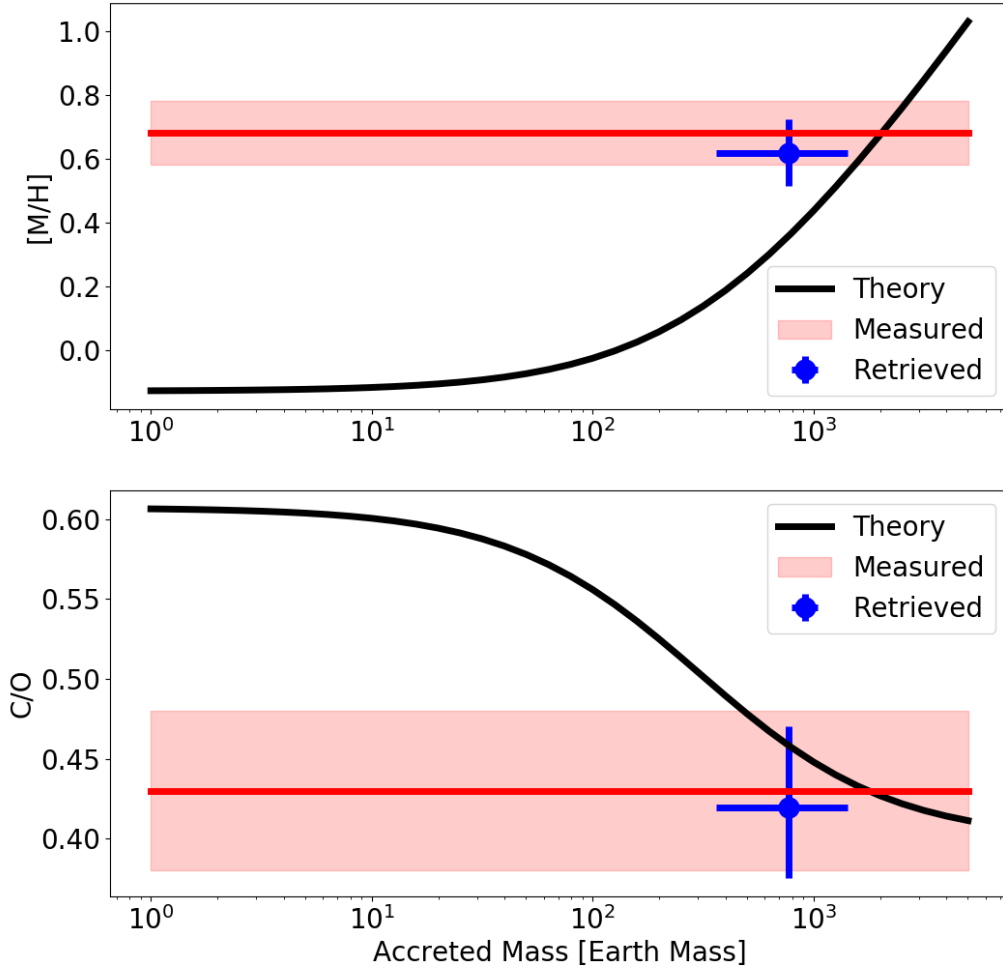


Figure 5. Illustration for how $\Delta[M/H]$ and C/O change with accretion mass and how the accretion mass (Blue data point with error bars) is determined by comparing model (Black solid curve) to observed values (red solid line and $1\text{-}\sigma$ band).